Eur. Phys. J. E **23**, 389–396 (2007)
DOI 10.1140/epje/i2007-10199-x

THE EUROPEAN PHYSICAL JOURNAL E

Confined ferrofluid droplet in crossed magnetic fields

D.P. Jackson[1,a] and J.A. Miranda[2,b]

[1] Department of Physics and Astronomy, Dickinson College, Carlisle, PA 17013, USA
[2] Departamento de Física-LFTC, UFPE, Recife, PE 50670-901, Brazil

Received 25 April 2007 and Received in final form 26 June 2007
Published online: 22 August 2007 –

Abstract. When a ferrofluid drop is trapped in a horizontal Hele-Shaw cell and subjected to a vertical magnetic field, a fingering instability results in the droplet evolving into a complex branched structure. This fingering instability depends on the magnetic field ramp rate but also depends critically on the initial state of the droplet. Small perturbations in the initial droplet can have a large influence on the resulting final pattern. By simultaneously applying a stabilizing (horizontal) azimuthal magnetic field, we gain more control over the mode selection mechanism. We perform a linear stability analysis that shows that any single mode can be selected by appropriately adjusting the strengths of the applied fields. This offers a unique and accurate mode selection mechanism for this confined magnetic fluid system. We present the results of numerical simulations that demonstrate that this mode selection mechanism is quite robust and "overpowers" any initial perturbations on the droplet. This provides a predictable way to obtain patterns with any desired number of fingers.

PACS. 47.65.Cb Magnetic fluids and ferrofluids – 47.15.gp Hele-Shaw flows

1 Introduction

Ferrofluids [1,2] are a class of soft material that can be easily manipulated by an applied magnetic field. They are colloidal suspensions of nanometer-sized magnetic particles suspended in a nonmagnetic carrier fluid. These magnetic fluids behave superparamagnetically and are distinguished by their ready response to even modest stimuli. Due to their sensitivity and responsiveness to applied magnetic fields, ferrofluids are well suited for exploring technological applications and for understanding fundamental scientific aspects of soft matter [3–6].

One interesting facet of ferrofluid research relates to the study of the interfacial patterns formed when it is in contact with a nonmagnetic fluid in the quasi-2D geometry of a Hele-Shaw cell. Depending on the nature and geometrical configuration of the applied magnetic field, it can either stabilize or destabilize the fluid-fluid interface. For such ferrohydrodynamic problems in a confined geometry the traditional Saffman-Taylor instability [7] is supplemented by a magnetically induced instability, leading to a variety of interfacial behaviors. In particular, if a strong magnetic field is applied perpendicular to the spatially constrained ferrofluid sample, the interfacial instability results in a highly convoluted, labyrinthine structure [8–11]. A destabilizing behavior is also observed by the simultaneous action of a uniform perpendicular field and an in-plane AC rotating magnetic field, which leads to the formation of amazing spiral and protozoan-like shapes [12–14]. On the other hand, the equally interesting stabilizing nature of the magnetic field can be revealed if it is applied in the plane of the Hele-Shaw cell, and parallel to the unperturbed fluid-fluid interface. In this case, one may observe the suppression of the Saffman-Taylor fingers in rectangular Hele-Shaw flow [15], the emergence of peculiar diamond-ring–shaped patterns in a rotating Hele-Shaw setup [16,17], or even the magnetic inhibition of interfacial cusp singularies in time-dependent gap Hele-Shaw cells [18,19].

The majority of studies investigating pattern formation of a ferrofluid confined in a Hele-Shaw cell focus on the competition between magnetic and nonmagnetic forces. For instance, in references [8–11] a perpendicular magnetic field acts to deform the ferrofluid interface while capillary or gravitational forces tend to keep it undisturbed (circular or planar). In contrast, in references [16–19] the magnetic field is stabilizing while the interface deformations are induced by centrifugal or lifting (nonmagnetic) forces. References [12–14] address the case in which two destabilizing magnetic fields (perpendicular and rotating) compete with surface tension forces.

In this work we study a different scenario and examine a situation in which the two major competing forces are both magnetic in nature. Specifically, we analyze the situation where a ferrofluid droplet is under the influence of

[a] e-mail: jacksond@dickinson.edu
[b] e-mail: jme@df.ufpe.br

two crossed magnetic fields: a (destabilizing) uniform perpendicular magnetic field, and a (stabilizing) nonuniform azimuthal magnetic field. The fact that the two relevant driving mechanisms are magnetically induced adds a welcome versatility to the system, allowing a more systematic way of manipulating the pattern formation phenomena via externally applied fields. This is in contrast to the majority of the confined ferrofluid problems in Hele-Shaw cells studied so far, in which the precise control of both magnetic and nonmagnetic forces is not as easy to implement. For example, while controlling the direction and intensity of applied magnetic fields is relatively easy, accurately controlling the surface tension between the fluids [20] or the angular velocity in a rotating Hele-Shaw cell [21,22] is not quite so simple.

The understanding and elucidation of the mechanisms of selection in the usual viscous fingering problem (using nonmagnetic fluids) has been a subject of lively discussion in the literature since the publication of the pioneering work by Saffman and Taylor [7]. Their problem is related to the more general subject of pattern selection in nonequilibrium phenomena, which has been of much subsequent interest [23–31]. However, similar studies involving magnetic fluids in Hele-Shaw cells have been largely neglected [32]. The purpose of the present work is to examine the pattern formation process of a ferrofluid in a Hele-Shaw geometry, and in particular, to investigate if the mode-selection mechanism can be conveniently and accurately regulated by applied magnetic fields. It turns out that because one has control over both the stabilizing and destabilizing forces, tuning the strengths of these two fields can be used to precisely control the pattern formation process. That is to say, one has the ability to drive any single mode, and *only* that mode, unstable.

The novelty of having such precise control over the pattern formation process should not be underestimated. This kind of control has not been previously observed even when both stabilizing and destabilizing forces have been present. For example, when a stabilizing azimuthal field is used in conjunction with a destabilizing centrifugal instability [16,17], one does obtain some control over the pattern selection mechanism. However, precise single-mode control is not possible. In this sense, the results presented here —from the simultaneous combination of both perpendicular and azimuthal fields— could not have been predicted based on any previous study. These results demonstrate a unique method of controlling pattern formation in this magnetic fluid system.

The paper is organized as follows: In Section 2 we perform a Fourier decomposition of the interface shape, and from a modified form of Darcy's law we study the combined influence of the crossed magnetic fields at early stages of pattern evolution. A linear stability analysis shows that the field strengths can be manipulated to allow any single mode to be driven unstable while all others are stable. The results of our linear analysis are further analyzed and probed in Section 3 through numerical simulations that confirm the ability to select any particular mode for growth. Our conclusions are summarized in Section 4.

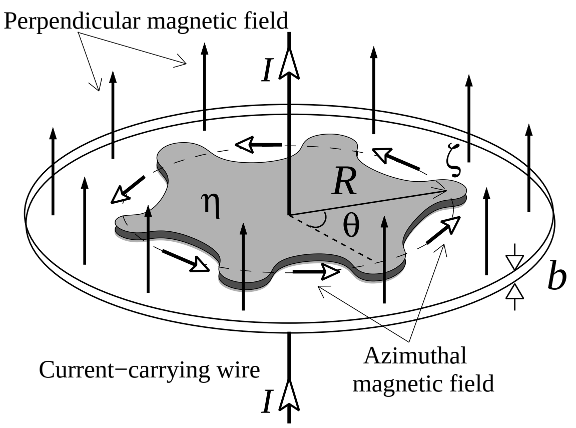

Fig. 1. A ferrofluid droplet in a Hele-Shaw cell simultaneously subjected to a uniform perpendicular magnetic field, and to an azimuthal magnetic field. The current-carrying wire passes through the center of the cell.

2 Linear stability results

Figure 1 illustrates a Hele-Shaw cell of thickness b, containing an initially circular droplet of ferrofluid of radius R and viscosity η, surrounded by a nonmagnetic fluid of negligible viscosity. The surface tension between the two fluids is given by σ. As in references [1,2,8–10] we assume that the ferrofluid is magnetized such that its magnetization $\mathbf{M}$ is collinear with the applied magnetic field. The system is under the influence of two crossed magnetic fields that are constant in time. The first is a uniform field acting perpendicular to the cell produced by a suitable solenoid or Helmholtz coil arrangement. This field is given by $\mathbf{H}_{\rm perp} = H_{\rm perp}\,\hat{\mathbf{e}}_z$, where $\hat{\mathbf{e}}_z$ is a unit vector pointing perpendicular to the Hele-Shaw cell. The second is an azimuthal field produced by a long straight, current-carrying wire that runs perpendicular to the Hele-Shaw cell. This field is given by $\mathbf{H}_{\rm azi} = I/(2\pi r)\,\hat{\mathbf{e}}_\theta$, where I denotes the constant electric current, r is the distance from the wire, and $\hat{\mathbf{e}}_\theta$ is a unit vector in the azimuthal direction.

The basic hydrodymanic equation for this system expresses the two-dimensional velocity field as given by a generalized Darcy's law [10,33]

$$\mathbf{v} = -\frac{b^2}{12\eta}\boldsymbol{\nabla}\Pi. \tag{1}$$

The generalized pressure $\Pi = P - \Psi$ contains both the (z-averaged) hydrodynamic pressure P and a magnetic pressure represented by a scalar potential $\Psi = \Psi_{\rm perp} + \Psi_{\rm azi}$. If we describe the ferrofluid boundary by a simple closed curve Γ parametrized by arclength s, then a convenient way of writing the perpendicular scalar potential is [10]

$$\Psi_{\rm perp} = \frac{\mu_0 R M_{\rm perp}^2}{2\pi b} J(s), \tag{2}$$

where μ_0 is the free-space permeability, $M_{\rm perp}$ is the magnetization created by the axial field (see App. A), and $J(s)$

is the (dimensionless) integral

$$J(s) = \frac{1}{R} \oint_{\Gamma} \mathrm{d}s' \, \hat{\mathbf{D}} \times \hat{\mathbf{t}}(s') \left[\sqrt{1 + (b/D)^2} - 1 \right]. \qquad (3)$$

Here, $\hat{\mathbf{t}}(s')$ is the unit tangent vector at arclength s' and $\hat{\mathbf{D}} = \mathbf{D}/D$ is a unit vector pointing in the direction of $\mathbf{D} = \mathbf{r}(s') - \mathbf{r}(s)$. In the azimuthal case, the scalar potential can be simply written as [17]

$$\Psi_{\mathrm{azi}} = \frac{\mu_0 \chi I^2}{8\pi^2 r^2}, \qquad (4)$$

where we have used the fact that $M_{\mathrm{azi}} = \chi H_{\mathrm{azi}}$, with χ representing the constant magnetic susceptibility.

It is worth mentioning that the magnetic body force which gives rise to the magnetic portion of equation (1) depends on the gradient of the local magnetic field. The local magnetic field can include contributions from the applied field as well as the demagnetizing field [1,2]. Here we consider only the lowest order effect of the magnetic interactions that would result in fluid motion. Thus, in the perpendicular situation, we include the demagnetizing field produced by the uniform magnetization resulting from the applied field. However, in the azimuthal situation, we consider only the applied field in determining the magnetization. This is well justified for ferrofluids of low magnetic susceptibility, and this will be assumed for the remainder of this paper. Finally, we note that it is possible to write the scalar potential Ψ as a sum of two parts (Ψ_{perp} and Ψ_{azi}) when the magnetization depends linearly on the total magnetic field (see App. A for more details regarding this point).

Before we specify the motion of the ferrofluid boundary, we note that since the fluid is incompressible, we have $\boldsymbol{\nabla} \cdot \mathbf{v} = 0$ and by virtue of equation (1), the generalized pressure obeys Laplace's equation $\nabla^2 \Pi = 0$. The boundary conditions are that the fluid velocity vanish at infinity and that the pressure at the boundary be given by

$$\Pi(s) \equiv \Pi\big|_{\Gamma} = \sigma\kappa - \Psi_{\mathrm{perp}}\big|_{\Gamma} - \Psi_{\mathrm{azi}}\big|_{\Gamma} - \frac{1}{2}\mu_0 M_n^2, \qquad (5)$$

with κ the boundary curvature and $\mu_0 M_n^2/2$ being the so-called magnetic normal traction [1, 2, 34]. The magnetic normal traction considers the influence of the normal component of magnetization at the ferrofluid boundary $M_n = \mathbf{M} \cdot \hat{\mathbf{n}}$. The motion of the boundary is then found using the kinematic boundary condition

$$\hat{\mathbf{n}} \cdot \frac{\partial \mathbf{r}}{\partial t}\bigg|_{\Gamma} = -\frac{b^2}{12\eta} \left(\hat{\mathbf{n}} \cdot \boldsymbol{\nabla} \Pi\big|_{\Gamma} \right). \qquad (6)$$

Notice that we need only specify the normal component of the boundary velocity as the tangential component has no physical significance. This flexibility will prove useful when implementing a numerical routine to solve for the ferrofluid evolutions.

Due to the action of the perpendicular field, a circular droplet may deform. To determine the stability of the ferrofluid boundary, we consider a slightly perturbed circle given by $\mathcal{R}(\theta, t) = R + \zeta(\theta, t)$, where $\zeta(\theta, t) = \zeta_n(t) \exp(in\theta)$ and n are the integer Fourier modes. Following the usual linear stability procedures [10,16,17,35], we obtain the differential equation for the Fourier perturbation amplitudes $\dot{\zeta}_n = \lambda(n)\zeta_n$, with the linear growth rates given by

$$\lambda(n) = \frac{b^2 \sigma n}{12\eta R^3} \left[\mathcal{D}_n(p) N_B^{\perp} - N_B - (n^2 - 1) \right], \qquad (7)$$

where

$$\mathcal{D}_n(p) = \frac{p^2}{2} \Bigg\{ \left[\psi\left(n + \frac{1}{2}\right) - \psi\left(\frac{3}{2}\right) \right] + \left[Q_{n-1/2}\left(\frac{p^2+2}{p^2}\right) - Q_{1/2}\left(\frac{p^2+2}{p^2}\right) \right] \Bigg\}, \qquad (8)$$

$N_B^{\perp} = \mu_0 b M_{\mathrm{perp}}^2/(2\pi\sigma)$ is the magnetic Bond number for the perpendicular field configuration, $p = 2R/b$ is the aspect ratio, and $N_B = \mu_0 \chi I^2/(4\pi^2 \sigma R)$ is the azimuthal magnetic Bond number. In equation (8), Q_n represents the Legendre function of the second kind, while Euler's psi-function ψ is the logarithmic derivative of the Gamma function. Notice that the function $\mathcal{D}_n(p) \geq 0$ for $n > 0$. Therefore, since the sign of the growth rate governs the interface stability, equation (7) tells us that the perpendicular (azimuthal) magnetic field will always destabilize (stabilize) the interface. Typical values of the material parameters (μ, χ, b, etc.) require perpendicular magnetic fields of order 10^{-2} Tesla to drive the system unstable [36]. This is fairly easy to accomplish with a Helmholtz coil arrangement and currents of a few amperes. An appropriate azimuthal field strength to stabilize the system would require currents of 100 A if a single wire is used; this current can be significantly reduced (to a few amperes) by using multiple wires in a loop configuration.

It is worth noting that the magnetic normal traction term in equation (5) does not affect the linear growth rates in equation (7). The lowest-order contribution of $\mu_0(\mathbf{M} \cdot \hat{\mathbf{n}})^2/2$, with $\hat{\mathbf{n}} = \boldsymbol{\nabla}[r - \mathcal{R}(\theta, t)]/|\boldsymbol{\nabla}[r - \mathcal{R}(\theta, t)]|$, is proportional to $(\partial\zeta/\partial\theta)^2$. Since this is second order in ζ, it is neglected in our linear analysis. This is simply a statement of the fact that to linear order, the magnetic normal traction acts as if the boundary of the ferrofluid were parallel to the azimuthal field.

Figure 2 shows the dimensionless linear growth rate $\tilde{\lambda}(n) = 12\eta R^3/(b^2\sigma)\lambda(n)$ as a function of mode number n for $p = 10$ and various $N_B^{\perp}$ and N_B. A few important features are seen from Figure 2. First, we see that larger values of $N_B^{\perp}$ lead to a larger band of unstable modes, larger growth rates, and the peak in the growth rate curve occurring for larger mode numbers. These features agree with similar results that have been previously observed in reference [10]. In addition, we see that increasing the azimuthal Bond number N_B leads to a smaller band of unstable modes, smaller growth rates, and a slight decrease in the peak of the growth rate curves. Of course, a large enough azimuthal field will stabilize the entire system.

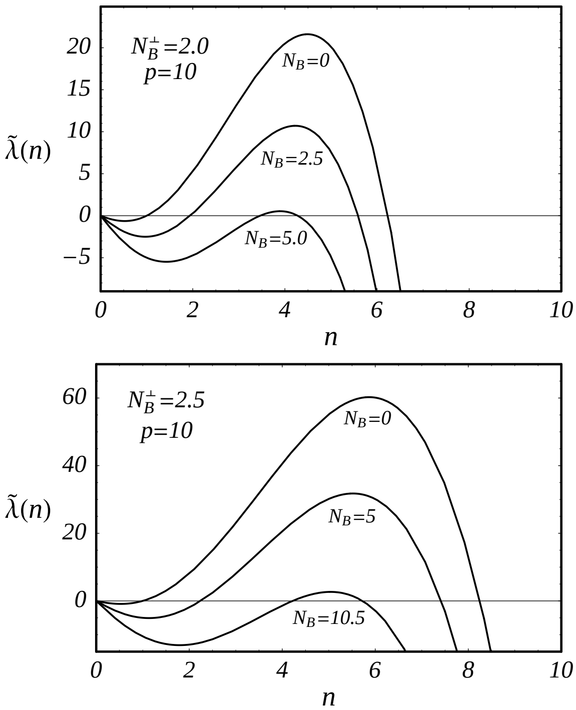

Fig. 2. Dimensionless linear growth rate $\tilde{\lambda}(n)$ as a function of Fourier mode n for $N_B^\perp = 2.0$ (top) and $N_B^\perp = 2.5$ (bottom) ($p = 10$ in both cases). Larger azimuthal Bond numbers N_B causes the band of unstable modes to shrink on both sides. An appropriate value for N_B leaves only a single unstable mode.

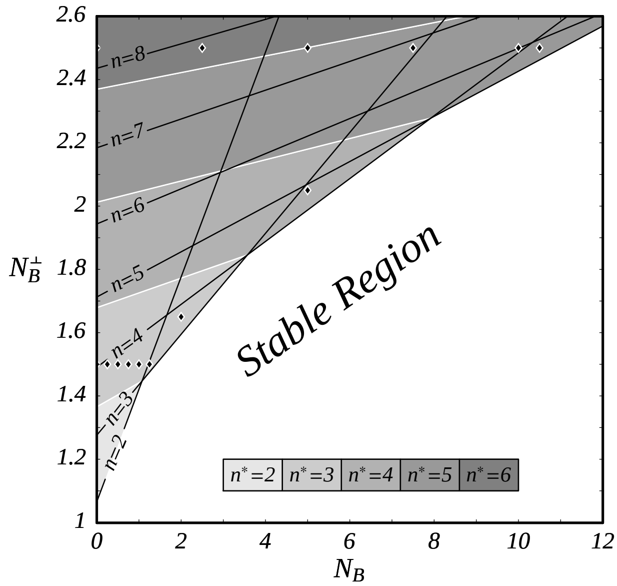

Fig. 3. Linear stability phase portrait showing neutral stability curves (solid black lines) and zones (shaded regions bounded by white lines) of fastest growing mode n^* for $p = 10$. The black diamonds show the values chosen for simulations as described in Section 3.

One immediate consequence of an azimuthal magnetic field should be to slightly reduce the number of fingers at the interface. In fact, this behavior was already expected from previous studies involving azimuthal fields [16, 17]. However, it is important to note that unlike the classical fingering problem in outward radial flow [37, 38] and the centrifugally-driven problem in rotating Hele-Shaw cells [21,39], here the band of unstable modes shrinks from *both* ends. This peculiar behavior allows one to tune the magnetic fields to produce a situation in which *any* mode can be selected as the *only* unstable mode. It is this unique feature that makes this such an interesting system. Here, we have the ability to fine tune the system to promote any specific mode we might want. This kind of selectivity could prove useful because it allows precise control over exactly what kinds of patterns are allowed to form.

All of the features we have been describing are contained in the growth rate equation. For example, the neutral stability curves for which $\lambda(n) = 0$ are found by setting equation (7) equal to zero. This results in

$$N_B^\perp = \frac{N_B + (n^2 - 1)}{\mathcal{D}_n(p)} \,. \tag{9}$$

Another useful quantity is the fastest growing mode n^*, defined as the (integer) mode that has the largest growth rate. This is the mode that will tend to dominate during the early stages of the pattern formation process and will perhaps determine the number of fingers in the final state. Now, a given mode n is only the fastest growing when $\lambda(n) > \lambda(n-1)$ and when $\lambda(n) > \lambda(n+1)$. Using equation (7), we find that the boundaries of the regions dominated by a particular mode n^* are given by

$$N_B^\perp = \frac{N_B + 3n^*(n^* \pm 1)}{[\mathcal{D}_{n^* \pm 1}(p)(1 \pm n^*) \mp n^* \mathcal{D}_{n^*}(p)]} \,. \tag{10}$$

A very useful way of organizing all the information contained in equations (9) and (10) is to make a linear stability phase portrait (Fig. 3). This figure shows the neutral stability curves for each mode as solid black lines and simultaneously shows the zones of fastest growing mode n^* as shaded regions separated by white lines. The black diamonds plotted in Figure 3 show the parameters used in some of our numerical simulations, to be discussed in Section 3.

Although Figure 3 contains a plethora of information, perhaps the most interesting feature of this graph is that the neutral stability curves cross each other. This makes it possible to go from the stable region to the unstable region by crossing the neutral stability curve of any mode one desires. In fact, as one crosses into the unstable region, there are triangular-shaped "islands" that represent regions where only a single mode is unstable. Thus, choosing parameters that lie inside one of these islands will allow you to specify precisely which mode is unstable. This convenient mode-selection feature is unique to this system and provides much more control than is possible in previous ferrofluid studies where the perpendicular and the azimuthal fields act separately [9, 10, 16, 17].

Studying Figure 3 further shows that in addition to regions with only a single unstable mode n, there are also regions where only modes n and $n-1$ are unstable. Perhaps not surprising is the fact that each of these (quadrilateral) regions is divided into sub-regions where mode n is fastest growing and where mode $n-1$ is fastest growing. Furthermore, one can find regions where modes n, $n-1$, and $n-2$ are the only unstable modes; where modes n, $n-1$, $n-2$, and $n-3$ are the only unstable modes; and continuing on to regions where modes n, $n-1$, $n-2\dots 4$, 3, and 2 are the only unstable modes. These last regions are located along the $N_B^{\perp}$ axis of Figure 3.

Most of the regions in Figure 3 with more than one unstable mode are divided into multiple sub-regions dominated by different fastest growing modes n^*. Others have only a single fastest growing mode throughout the entire region. To what extent this affects the pattern formation process is discussed in the next section.

3 Numerical simulations

Although our linear analysis provides a significant amount of interesting information, linear theory is only valid for the very early stages of the pattern formation process. Of course, in some situations, linear theory can still be an excellent predictor of certain features of the patterns that form. One such example is how the interactions of multiple domains can affect the pattern formation process [40–42].

To explore beyond the early stages of the pattern formation process, we turn to numerical evolutions of the equations of motion. As described in Section 2, the motion of the ferrofluid boundary is specified only by the normal component of the generalized pressure gradient at the boundary (6). The pressure field is found by solving Laplace's equation on an arbitrarily shaped (simply connected) domain with a specified value (5) on the boundary. Thus, we need to solve a Dirichlet problem on an arbitrarily shaped domain that evolves in time. Our basic approach is to use a conformal mapping algorithm to map the domain of interest (the z-plane) to the unit disk (the ω-plane) where the solution is given by the Poisson integral formula. The Riemann mapping theorem guarantees that such a map always exists. This method specifies a particular tangential velocity to maintain the analyticity of the mapping function for all time [23].

If $z = f(t,\omega)$ is the map that takes you from the ω-plane to the z-plane at time t, then the boundary of the ferrofluid domain is given by $\gamma(t,s) = f(t,e^{is})$. After rescaling time by $12\eta R^3/(b^2\sigma)$, the equation of motion for the ferrofluid is given by [10]

$$\frac{\partial \gamma}{\partial t} = -\omega\partial_\omega f \mathcal{A}\left\{\frac{\mathrm{Re}\left[\omega\partial_\omega \mathcal{A}\left\{\tilde{\Pi}(s)\right\}\right]}{|\omega\partial_\omega f|^2}\right\}, \tag{11}$$

where ω lies on the unit circle and $\tilde{\Pi}(s)$ is a dimensionless version of equation (5) given by

$$\tilde{\Pi}(s) = \tilde{\kappa} - \frac{1}{4}p^2 N_B^{\perp} J(s) - \frac{1}{2}\frac{N_B}{\tilde{r}^2}\left[1+\chi(\hat{\mathbf{n}}\cdot\hat{\mathbf{e}}_\theta)^2\right], \tag{12}$$

with $\tilde{\kappa}$ and $\tilde{r}$ dimensionless variables that have been rescaled by the radius of the initial ferrofluid drop R. In equation (11), $\mathcal{A}\{\cdots\}$ is an integral operator that acts on a real-valued function $g(s)$ and returns a complex function that is analytic inside the unit disk and whose real part on the boundary is $g(s)$. That is, given a real function

$$g(s) = \sum_{n=0}^{\infty}\left(a_n e^{ins} + a_n^* e^{-ins}\right), \tag{13}$$

then

$$\mathcal{A}\{g(s)\} = 2\sum_{n=0}^{\infty} a_n z^n. \tag{14}$$

Because the operator $\mathcal{A}$ can be simply written in terms of the Fourier coefficients a_n, these calculations can be done using fast Fourier transform routines. The bottleneck in the routine is in the calculation of the integrals given in equation (3) for each point on the interface.

We also note that the magnetic traction term in equation (12) arises solely from the azimuthal magnetic field and provides a stabilizing influence with a similar functional form as the other azimuthal magnetic field term. Since the traction term is multiplied by the magnetic susceptibility χ (assumed small), we have neglected the final term in equation (12). This simplifies the computations considerably and should have very little effect on the resulting patterns.

As previously mentioned, one of the most interesting features arising in the linear analysis is the ability to specify the two control parameters, N_B and $N_B^{\perp}$, so that there is only a single unstable mode. A natural question to ask is if there is only a single unstable mode, does the "final state" pattern (stable pattern after the evolution has stopped) bear the signature of this mode in some way? Perhaps the final-state pattern will have precisely the same number of fingers as the initial mode of instability. While this may seem like a natural expectation, it is not at all certain that this should be the case because the equation of motion (11) is highly nonlinear. These nonlinearities can lead to mode competition that can result in the number of fingers being different from what might naively be expected based on linear theory alone [10, 16, 43]. On the other hand, in this situation, there should not be any mode competition at all since there is only a single unstable mode.

To explore this possibility, we numerically evolve the equation of motion (11) using appropriate values for the control parameters that produce only a single unstable mode. When possible, these points are plotted on the phase portrait in Figure 3. Figure 4 shows the results of these simulations for $p = 10$ when the only unstable modes are $n = 3$, 4, 5, and 6. One can immediately see that the final-state patterns have exactly the same number of fingers as the initial mode of instability. This agrees perfectly with the predictions of the linear analysis. For each of these simulations, we begin with a slightly perturbed circle that consists of small random amplitudes added to the first eight Fourier modes. It is important to note that the exact same initial condition is used for all of the simulations shown in Figure 4. Thus, the fact that

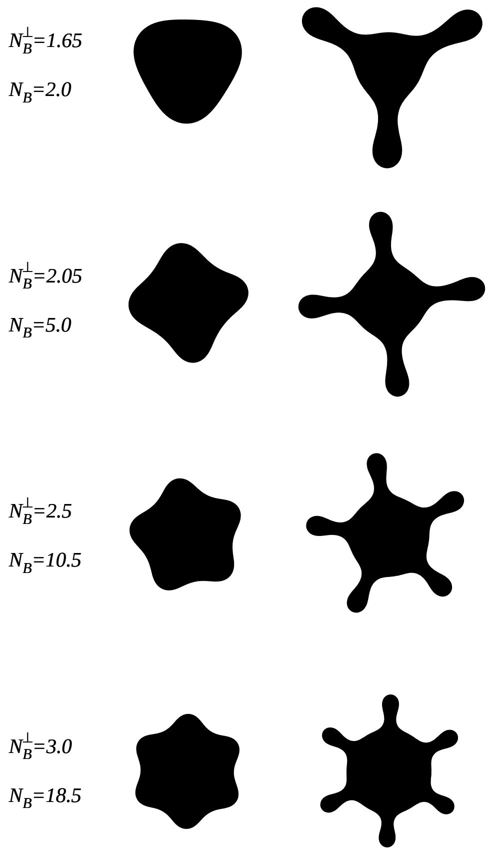

Fig. 4. Numerical evolutions of the equation of motion (11) with $p = 10$ and various N_B and $N_B^{\perp}$ using the exact same initial condition (a slightly noisy circle). The Bond numbers, chosen so that there is only a single unstable mode in each case, are plotted in Figure 3 when possible. The left column shows the early stages of the evolution and the right column shows the final-state patterns.

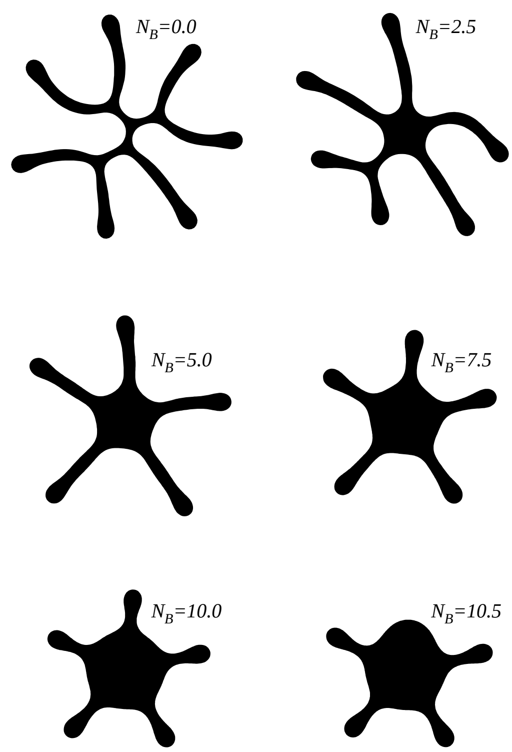

Fig. 5. Numerical evolutions with $p = 10$, $N_B^{\perp} = 2.5$, and various values for N_B (plotted in Fig. 3). A different initial condition was used here compared to those shown in Figure 4.

each simulation ends with a different number of fingers cannot be attributed to the initial conditions.

In addition to testing the linear theory when only a single mode is unstable, we also run simulations with a fixed value of $N_B^{\perp} = 2.5$ while changing the values of N_B (still with $p = 10$). In this way we see how the application of the stabilizing azimuthal magnetic field affects the final-state pattern produced by the perpendicular magnetic field. Figure 5 shows the results of these simulations. When $N_B = 0$, we see a familiar pattern formed from the perpendicular field alone. This particular pattern is in excellent agreement with the corresponding shapes obtained experimentally [9,10,43]. Reference to Figure 3 shows that for $N_B^{\perp} = 2.5$ and $N_B = 0$ modes 2 through 8 are all unstable and $n = 6$ is the fastest growing mode. Therefore, one might naively expect that the final-state pattern should have six fingers. In contrast to this prediction, Figure 5 shows that the final-state pattern for this case has 7 fingers. This discrepancy has been noted and a fairly successful description of early finger formation was proposed to accommodate these observations [10].

Referring back to Figure 5, we see that as N_B is increased, the number of fingers in the final-state pattern is observed to decrease. This agrees qualitatively with the linear phase portrait shown in Figure 3. Not only does the fastest growing mode decrease as N_B increases, but the actual modes that are unstable changes as well. First mode 8 becomes stable, then mode 2, then modes 7, 3, 6, and 4 become stable (in this order). This finally leaves the single unstable mode $n = 5$. We also note that as N_B increases, the fingers become much less curved and are more radially oriented. We believe this is a result of less mode competition during the pattern formation process. The fewer unstable modes that are available as N_B increases means the pattern formed early in the evolution is likely to attain a more symmetrical appearance. Although not perfect, this symmetry is clearly visible in the left column of Figure 4 when there is only a single unstable mode.

Interestingly, although $n = 5$ is the only unstable mode in the final simulation in Figure 5 (with $N_B^{\perp} = 2.5$ and $N_B = 10.5$), the final-state pattern has only four well-developed fingers. This is in contrast to what is shown in Figure 4. The reason for the difference is that we used a different initial condition for the set of simulations shown in Figure 5. Thus, just because there is only a single unstable mode does not necessarily mean that the final-state pattern will have exactly that number of fingers. The pattern will begin developing with precisely that number of

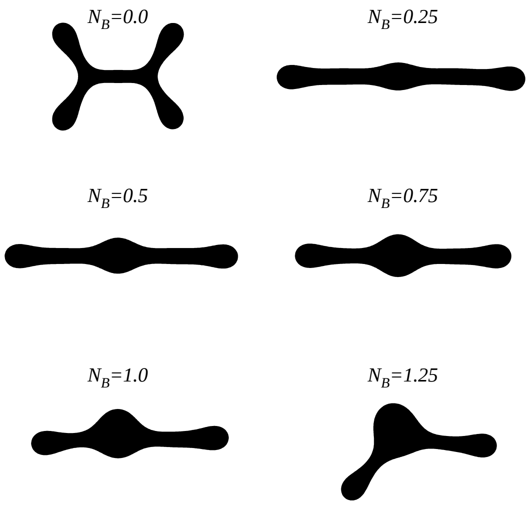

Fig. 6. Numerical evolutions with $p = 10$, $N_B^{\perp} = 1.5$, and various values for N_B (plotted in Fig. 3). The initial condition was a small amplitude $n = 2$ Fourier mode. Notice that the initial condition does not appear to have an impact on the final-state pattern after this mode has become stable (when $N_B = 1.25$).

fingers but small differences in the initial conditions can lead to one or more of these fingers disappearing by the time the evolution stops.

In addition to simulations with random initial conditions, we also run some simulations with a prescribed initial condition of a particular Fourier mode to see whether this perturbation would have an impact on the final-state pattern even when this Fourier mode was stable. Figure 6 shows the results of these simulations with $p = 10$, $N_B^{\perp} = 1.5$, and various values of N_B (plotted in Fig. 3 as before). The initial condition was a small amplitude $n = 2$ mode aligned in the left-right direction. When $N_B = 0$, modes 2, 3, and 4 are all unstable, and although $n = 3$ is the fastest growing mode, the final-state pattern ends up with four fingers and reflects the left-right symmetry of the initial condition. When $N_B = 0.25$, the $n = 4$ mode is no longer stable and although the $n = 3$ mode is still the fastest growing mode, the final-state pattern has only two fingers and still reflects the initial condition. We also note that there is a small bulge near the center of the pattern. This is because the stabilizing azimuthal field acts to pull the fluid in toward the origin.

As N_B is increased further, the length of the fingers decreases as more and more of the fluid is drawn towards the central region. Then, when $N_B = 1.25$, the $n = 2$ mode becomes stable, leaving mode $n = 3$ as the only unstable mode. Although the final-state pattern has only two fingers, the symmetry of the pattern no longer reflects the symmetry of the initial condition but instead reflects the symmetry of the mode-3 instability. Thus, we see that as in Figure 4, the initial conditions can be overridden when there is only a single unstable mode available to seed the growth of the pattern.

4 Conclusion

In this work we have studied the evolution of a confined ferrofluid droplet in the presence of two crossed magnetic fields: perpendicular (destabilizing) and azimuthal (stabilizing). This particular setup differs from previous pattern-forming investigations in a very important aspect —the two major competing forces are both magnetic in nature. This provides a large amount of control over the pattern formation process and in some cases allows us to predict with relative certainty the morphology of the final patterns. This predictability comes about because the band of unstable modes shrinks from both ends as the azimuthal field is increased. Thus, the magnetic fields can be specifically tuned so that any particular mode —and *only* that mode— can be driven unstable. This mode-selection mechanism is not only precise but is also robust enough to overcome any preference resulting from the initial perturbations on the ferrofluid drop. Furthermore, these initial instabilities have a dramatic impact on the final-state patterns as demonstrated with our numerical results.

Our theoretical work makes specific predictions that have not been investigated experimentally. We are very interested in seeing our predictions tested with actual experiments, and hope the results presented here will encourage some investigators to attempt these experiments.

This type of pattern selectivity could prove very useful in other pattern-forming systems including dendritic solidification [44, 45] and electrochemical deposition [46–48] among others. Recent experimental works [49, 50] have demonstrated that the presence of external magnetic fields during pattern formation in electrochemical growth can lead to very different arborescent morphologies. When submitted to the combined action of perpendicular and azimuthal magnetic fields, these electrochemical growth systems could be promising candidates to test the mode-selection mechanism we discuss here for confined magnetic fluids. Finally, we point out that very recent numerical simulations describing the flow of miscible ferrofluids in lifting Hele-Shaw cells (under the action of crossed magnetic fields) [51] also indicate the existence of a similar mode-selection scheme.

J.A.M. thanks CNPq (Brazilian Research Council) for financial support of this research through the program “Instituto do Milênio de Fluidos Complexos” contract No. 420082/2005-0. D.P.J. thanks Dickinson College for financial support of this research.

Appendix A. Magnetic body force and Darcy’s law under crossed magnetic fields

Here we would like to discuss a few important points related to the usefulness and validity of equation (1) when the azimuthal and the perpendicular magnetic fields act simultaneously (crossed-field situation). In general, if the ferrofluid magnetization function is nonlinear with the total magnetic field, one cannot simply add the separate magnetic force components together as expressed in our generalized Darcy's law (Eq. (1)): the magnetic fields themselves certainly obey linear superposition, but the magnetization may not. Thus, it is important to clarify under what conditions equation (1) is valid in the crossed-field case.

We begin with the magnetic body force, which can be written as [1,2]

$$\boldsymbol{F}_m = \mu_0 M \boldsymbol{\nabla} H, \tag{A.1}$$

where $M = |\mathbf{M}|$ is the magnitude of the magnetization and $H = \sqrt{H_{\text{perp}}^2 + H_{\text{azi}}^2}$ is the magnitude of the total magnetic field. If we consider a linear relationship $\mathbf{M} = \chi \mathbf{H}$, where χ is the constant magnetic susceptibility, then equation (A.1) can be easily rewritten as

$$\boldsymbol{F}_m = \mu_0 \chi \frac{1}{2} \boldsymbol{\nabla} H^2 \tag{A.2}$$

$$= \mu_0 M_{\text{perp}} \boldsymbol{\nabla} H_{\text{perp}} + \mu_0 M_{\text{azi}} \boldsymbol{\nabla} H_{\text{azi}}\,, \tag{A.3}$$

where $M_{\text{perp}} = \chi H_{\text{perp}}$ and $M_{\text{azi}} = \chi H_{\text{azi}}$. Equation (A.3) immediately tells us that the magnetic body force is simply the sum of the "perpendicular body force" and the "azimuthal body force." Then, using a fairly standard approach (see for instance, Refs. [1,2,8–11,16,17,52]), we introduce scalar potentials and average over the gap height to obtain equation (1).

References

1. R.E. Rosensweig, *Ferrohydrodynamics* (Cambridge University Press, Cambridge, 1985).
2. E. Blums, A. Cebers, M.M. Maiorov, *Magnetic Fluids* (de Gruyter, New York, 1997).
3. B. Berkovski, *Magnetic Fluids and Applications Handbook* (Begell House, New York, 1996).
4. J.-C. Bacri, R. Perzynski, D. Salin, Endeavour **12**, 76 (1988).
5. M. Seul, D. Andelman, Science **267**, 476 (1995).
6. M. Zahn, J. Nanopart. Res. **3**, 73 (2001).
7. P.G. Saffman, G.I. Taylor, Proc. R. Soc. London, Ser. A **245**, 312 (1958).
8. A.O. Tsebers, M.M. Maiorov, Magnetohydrodynamics **16**, 21 (1980).
9. S.A. Langer, R.E. Goldstein, D.P. Jackson, Phys. Rev. A **46**, 4894 (1992).
10. D.P. Jackson, R.E. Goldstein, A.O. Cebers, Phys. Rev. E **50**, 298 (1994).
11. G. Pacitto, C. Flament, J.-C. Bacri, M. Widom, Phys. Rev. E **62**, 7941 (2000).
12. C. Lorenz, M. Zahn, Phys. Fluids **15**, S4 (2003).
13. S. Rhodes, J. Perez, S. Elborai, S.-H. Lee, M. Zahn, J. Magn. & Magn. Mater. **289**, 353 (2005).
14. S. Elborai, D.-K. Kim, X. He, S.-H. Lee, S. Rhodes, M. Zahn, J. Appl. Phys. **97**, 10Q303 (2005).
15. M. Zahn, R.E. Rosensweig, IEEE Trans. Magn. **16**, 275 (1980).
16. D.P. Jackson, J.A. Miranda, Phys. Rev. E **67**, 017301 (2003).
17. J.A. Miranda, Phys. Rev. E **62**, 2985 (2000).
18. J.A. Miranda, R.M. Oliveira, Phys. Rev. E **69**, 066312 (2004).
19. R.M. Oliveira, J.A. Miranda, Phys. Rev. E **73**, 036309 (2006).
20. C. Flament, S. Lacis, J.-C. Bacri, A. Cebers, S. Neveu, R. Perzynski, Phys. Rev. E **53**, 4801 (1996).
21. Ll. Carrillo, F.X. Magdaleno, J. Casademunt, J. Ortín, Phys. Rev. E **54**, 6260 (1996).
22. E. Alvarez-Lacalle, J. Ortín, J. Casademunt, Phys. Fluids **16**, 908 (2004).
23. D. Bensimon, L.P. Kadanoff, S. Liang, B.I. Shraiman, C. Tang, Rev. Mod. Phys. **58**, 977 (1986).
24. P.G. Saffman, J. Fluid Mech. **173**, 73 (1986).
25. D.A. Kessler, H. Levine, Phys. Rev. A **33**, 2621; 2634 (1986).
26. M. Mineev-Weinstein, Phys. Rev. Lett. **80**, 2113 (1998).
27. M. Mineev-Weinstein, P.B. Wiegmann, A. Zabrodin, Phys. Rev. Lett. **84**, 5106 (2000).
28. J. Casademunt, F.X. Magdaleno, Phys. Rep. **337**, 1 (2000).
29. D.A. Kessler, H. Levine, Phys. Rev. Lett. **86**, 4532 (2001).
30. O. Agam, E. Bettelheim, P. Wiegmann, A. Zabrodin, Phys. Rev. Lett. **88**, 236801 (2002).
31. L. Ristroph, M. Thrasher, M.B. Mineev-Weinstein, H.L. Swinney, Phys. Rev. E **74**, 015201(R) (2006).
32. G. Pacitto, C. Flament, J.-C. Bacri, Phys. Fluids **13**, 3196 (2001).
33. A.O. Tsebers, Magnetohydrodynamics **17**, 113 (1981).
34. J.A. Miranda, R.M. Oliveira, D.P. Jackson, Phys. Rev. E **70**, 036311 (2004).
35. J.A. Miranda, M. Widom, Phys. Rev. E **55**, 3758 (1997).
36. N.J. Hillier, D.P. Jackson, Phys. Rev. E **75**, 036314 (2007).
37. L. Paterson, J. Fluid Mech. **113**, 513 (1981).
38. J.A. Miranda, M. Widom, Physica D **120**, 315 (1998).
39. L.W. Schwartz, Phys. Fluids A **1**, 167 (1989).
40. D.P. Jackson, B. Gantner, Phys. Rev. E **64**, 056230 (2001).
41. D.P. Jackson, Phys. Rev. E **68**, 035301(R) (2003).
42. D.P. Jackson, J. Magn. & Magn. Mater. **289**, 188 (2005).
43. A.J. Dickstein, S. Erramilli, R.E. Goldstein, D.P. Jackson, S.A. Langer, Science **261**, 1012 (1993).
44. J.S. Langer, Science **243**, 1150 (1989).
45. D. Kesser, H. Levine, J. Koplik, Adv. Phys. **37**, 255 (1988).
46. M. Matsushita, M. Sano, Y. Hayakawa, H. Honjo, Y. Sawada, Phys. Rev. Lett. **53**, 286 (1984).
47. Y. Sawada, A. Dougherty, J.P. Gollub, Phys. Rev. Lett. **56**, 1260 (1986).
48. D. Grier, E. Ben-Jacob, R. Clarke, L.M. Sander, Phys. Rev. Lett. **56**, 1264 (1986).
49. S. Bodea, L. Vignon, R. Ballou, P. Molho, Phys. Rev. Lett. **83**, 2612 (1999).
50. S. Bodea, R. Ballou, P. Molho, Phys. Rev. E **69**, 021605 (2004).
51. C.-Y. Chen, S.-Y. Wu, J.A. Miranda, Phys. Rev. E **75**, 036310 (2007).
52. J. Richardi, D. Ingert, M.P. Pileni, Phys. Rev. E **66**, 046306 (2002).